Contents lists available at ScienceDirect

Earth and Planetary Science Letters

Radial thermo-chemical structure beneath Western and Northern Pacific from seismic waveform inversion

Frédéric Deschamps [a,*], Kensuke Konishi [a], Nobuaki Fuji [b], Laura Cobden [c]

[a] *Institute of Earth Sciences, Academia Sinica, 128 Academia Road, 11529 Taipei, Taiwan*
[b] *Institut de Physique du Globe de Paris, 1 rue Jussieu, 75238 Paris cedex 05, France*
[c] *Department of Earth Sciences, Utrecht University, Princetonlaan 8a, 3584CB, Utrecht, The Netherlands*

A B S T R A C T

The Earth's deep mantle seismic structure is dominated by two large low shear-wave velocity provinces (LLSVPs) located beneath Africa and the Pacific. While the existence of these structures has been attested by many studies and data sets, their detailed nature, purely thermal or thermo-chemical, is still a matter of debate. Discriminating between these hypotheses requires constraints independent from seismic velocity structure. Seismic shear-wave attenuation, measured by the quality factor Q_S, strongly depends on temperature but not (or weakly) on composition. It may bring key information on temperature, resolving in turn the trade-off between temperature and composition. Here, we invert seismic waveform data for radial models of shear-wave velocity anomalies ($d\ln V_S$), and Q_S at two different locations in the Pacific, and from a depth of 2000 km down to the core-mantle boundary (CMB). We show that Western Pacific (WP) models, sampling the western tip of the Pacific LLSVP and the Caroline plume, cannot be explained by thermal anomalies alone, but require excess in iron of ∼4.0% from the CMB up to 2600 km. By contrast, Northern Pacific models (NP), if unaffected by seismic anisotropy, may have a purely thermal origin. Based on these observations, we build radial thermo-chemical models at WP and NP.

© 2019 Elsevier B.V. All rights reserved.

1. Introduction

The large scale thermo-chemical structure of Earth's deep mantle is still debated, a central question being the nature of the large low shear-wave velocity provinces (LLSVPs) mapped by seismic tomography beneath Africa and the Pacific (Garnero et al., 2016). These structures have been observed by studies based on various datasets, including traveltime (see Ritsema et al., 2011 for a comparison of different models), waveform (French and Romanowicz, 2015; Bozdağ et al., 2016), and normal mode (Trampert et al., 2004; Moulik and Ekström, 2016) data, and thus appear as robust features. By contrast, their nature, purely thermal or thermo-chemical, is still unclear. While several observations, among which the anti-correlation between shear-wave and bulk sound seismic velocities (Masters et al., 2000; Trampert et al., 2004), strongly favour a thermo-chemical origin, other studies have suggested that observed differential traveltimes may result from complexities of wave-propagation through purely thermal structures (Schuberth et al., 2012), or be explained by the presence of post-perovskite around hot regions (Davies et al., 2012; Hutko et al., 2008). It has

further been pointed out that given the resolution of current tomographic models, LLSVPs may be equally well explained by plume clusters or thermo-chemical piles (e.g., Bull et al., 2009).

This lack of consensus is largely due to the fact that seismic velocity anomalies alone cannot simultaneously resolve the thermal and compositional contributions from which they originate. Discriminating between purely thermal and thermo-chemical scenarios requires constraints independent from seismic velocity structure. The mapping of density from normal modes provided constraints that globally support the thermo-chemical hypothesis (Trampert et al., 2004; Mosca et al., 2012). Similarly, the 6-year periodic variations in the length-of-day and surface deformation, which are well explained by gravitational coupling between the inner core and the lowermost mantle (Ding and Chao, 2018), and the deformation measurements of semi-diurnal body tides (Lau et al., 2017) imply mass excess in regions overlapping LLSVPs. Stoneley mode measurements, by contrast, concluded that LLSVPs may be less dense than surrounding mantle (Koelemeijer et al., 2017). Seismic attenuation, measured with seismic quality factor, strongly depends on temperature (Anderson and Given, 1982). Attenuation may further depend on water content, but this contribution can be neglected in the lowermost mantle (Panero et al., 2015). Combined with seismic wave speeds, seismic attenuation may thus

---

help to separate the thermal and compositional signals contained in seismic data. So far, however, no study has attempted to infer lowermost mantle thermo-chemical structure jointly from seismic wave speeds and attenuation. Here, we combine the radial models of shear-wave speed (V_S) and seismic shear-wave attenuation obtained by Konishi et al. (2017) beneath the Western Pacific together with new models sampling the deep mantle beneath the Northern Pacific and using the same waveform inversion technique, to constrain the thermo-chemical structure at these two locations.

2. Radial models of shear-wave speed and seismic attenuation

We first inverted seismic waveform data for radial models of shear-wave speed anomaly ($dlnV_S$) with respect to PREM (Dziewonski and Anderson, 1981) and shear-wave quality factor Q_S at depths ranging from 2000 km down to the core-mantle boundary (CMB) beneath the western tip of the Pacific LLSVP and beneath the Northern Pacific. Western Pacific models are taken from Konishi et al. (2017) (central region), while Northern Pacific profiles are computed for this study. Note that, we only inverted for the transverse component (*SH*-wave) of the shear-wave speed structure.

2.1. Data and inversion method

Western Pacific (WP) models were built using 1341 *ScS* waveforms from 31 earthquakes (Supplementary Table S1) that occurred in the Tonga-Fiji region and were recorded by the Japanese seismic network F-net (77 stations), leading to epicentral distances in the range 75–85°. This dataset samples the western tip of the Pacific LLSVP, a region associated with the Caroline plume (French and Romanowicz, 2015; Bozdağ et al., 2016) and where V_S is strongly reduced compared to PREM (Fig. 1a), with anomalies around −2.3% in S40RTS (Ritsema et al., 2011), and −3.1% in SEMUC-WM1 (French and Romanowicz, 2015). Northern Pacific (NP) models were computed using 601 waveforms from 11 earthquakes (Supplementary Table S2) that occurred in Japan and Mariana trenches and were recorded by the USArray seismic network (294 stations), leading to epicentral distances in the range 80–90°. They sample a region where V_S is close to PREM (Fig. 1b), with anomaly of −0.1% in S40RTS (Ritsema et al., 2011), and can be used, by comparison, to infer the physical causes of the deviations observed in WP models. Fig. 1 shows the geometry of sources and seismic stations, and Fig. 2 plots selected waveforms. For both datasets, we performed static corrections with both *S* and *ScS* phases to eliminate near-source and near-receiver effects related to local structures in the crust or shallow mantle (Supplementary Material). Data are then sampled up to 20 Hz and filtered between 0.005 and 0.08 Hz, corresponding to the period range 12.5–200 s. Based on regional trends (Supplementary Material, Fig. S1), we split WP dataset into three sub-datasets and inverted each of them independently, leading to three radial models. Here, we only use the central model, which is based on 814 *ScS* waveforms. At NP, the dataset is homogeneous, and we inverted it as a whole.

To build our models, we use the seismic full waveform inversion described in Konishi et al. (2017), to which we refer for technical details. For clarity, we briefly summarize the main points below and give further details in Supplementary Material. Our 1-D *ScS* waveform inversion method is designed to minimize L2-norm misfit between synthetic and observed waveforms. Synthetics were computed with the direct solution method (DSM) (Geller and Ohminato, 1994). Importantly, DSM computes wave propagation governed by the equation of motion, and thus includes all waveform perturbations accountable by the equation of motion,
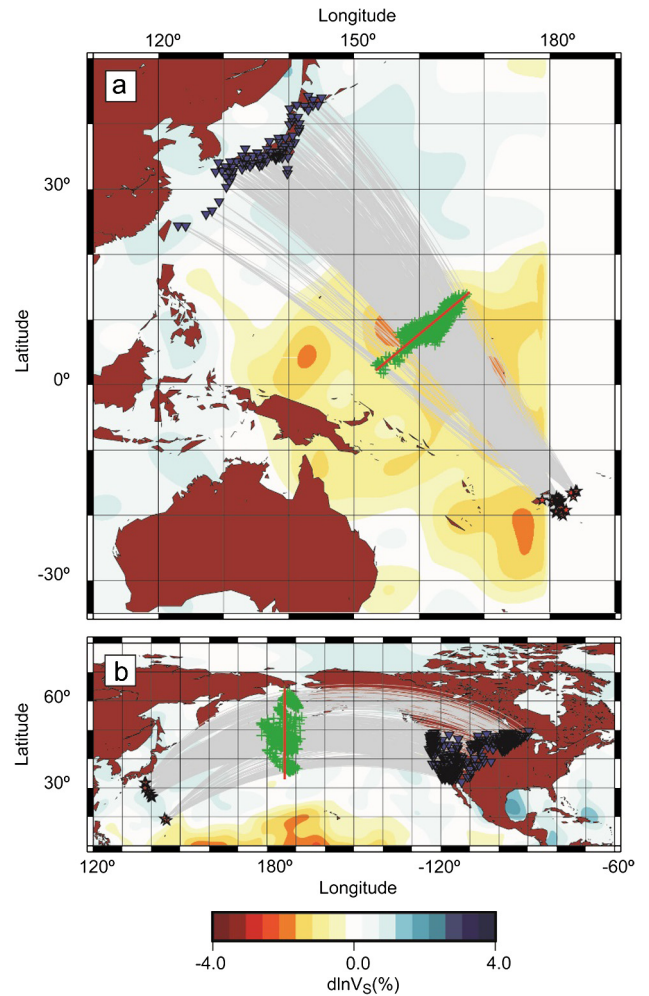

Fig. 1. Geometrical distribution of seismic events (red stars) and stations (blue triangles) with great circle ray paths (grey curves) and bounce points (green crosses) for (a) Western Pacific (WP) and (b) Northern Pacific (NP) models. Red segments show the regression lines of the bounce points. WP dataset was split into three different sub-datasets leading to three sets of models. Here we use only the WP central models. Background maps plot the lowermost layer of tomographic model S40RTS (Ritsema et al., 2011).

for instance scattering triggered by sharp velocity changes. Synthetics are then convolved with source-time functions estimated from the data set, sampled to 20 Hz, and filtered in the same frequency range as for real data, i.e. 0.005–0.08 Hz.

Waveform inversion is based on a Taylor expansion of a perturbed starting 1-D model, here PREM (Dziewonski and Anderson, 1981) in the case of NP, and PREM' in the case of WP. PREM' is an *ad-hoc* 1-D model modified from PREM and representative of the shear-wave velocity in the deep mantle beneath the Western Pacific (Konishi et al., 2009). It is equal to PREM down to 2500 km, and is set constant to 7.15 km/s at greater depths, resulting in a relative anomaly (with respect to PREM) of −1.5% at the CMB. The use of PREM' as starting model facilitates the inversion for WP models. The linearized problem solves a set of normal equations given by

$$\mathbf{A^T A \delta m = A^T \delta d,} \tag{1}$$

where δm and δd are the model and data vectors, and **A** the matrix of partial derivatives of displacement with respect to elastic constants and anelastic parameters (Fuji et al., 2010). Again, it is important to keep in mind that these derivatives account for wave-propagation effects, in particular scattering effects. Sensitiv-
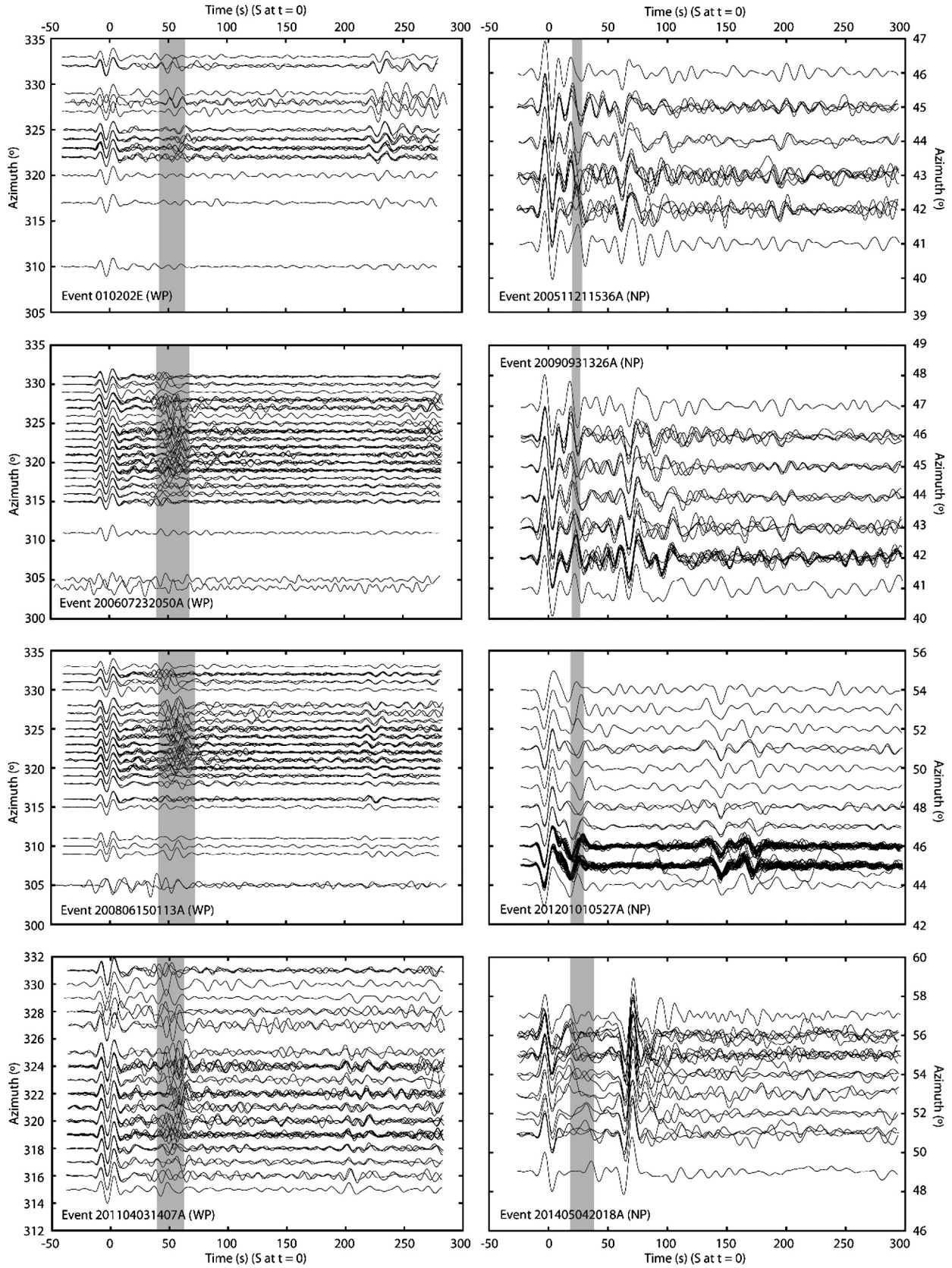
Fig. 2. Selected waveforms for Western Pacific (WP, left column) and Northern Pacific (NP, right column) datasets. Traces are aligned with *S*-wave arrival at $t = 0$. The delay time of the midpoint between positive and negative peaks of the *ScS* phase ranges from 32.2 to 72.4 s at WP and from 18.1 to 57.4 s at NP. The individual ranges for each event are indicated with grey bands. The large amplitude arrival after the *ScS* phase on NP event 201405041018A is an *sS* phase.
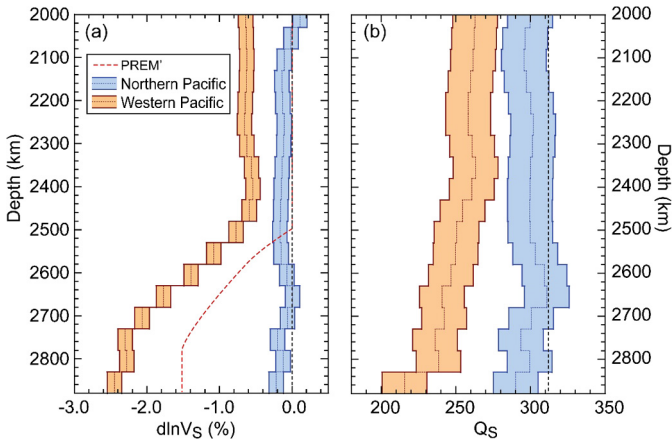
Fig. 3. Models of (a) shear-wave speed anomalies (dlnV_S) and (b) seismic shear-wave quality factor (Q_S) for regions sampling the Northern Pacific (blue curves and coloured areas), and the western tip of the Pacific LLSVP (red/orange curves and coloured areas). Anomalies dlnV_S are relative to PREM at both locations, and the dashed line in plot b indicates the Q_S value of PREM, $Q_{PREM} = 312$ (Dziewonski and Anderson, 1981). Coloured areas denote the possible uncertainties in each model, estimated from resolution and bootstrap tests (Fig. 4 and Supplementary Fig. S3). The red dashed line in plot a shows the model PREM', which is used as starting model for inversion of Western Pacific models.

ity kernels (Supplementary Fig. S2), here calculated for PREM, are given by the diagonals of the Hessian matrix, defined by the product $\mathbf{A}^T\mathbf{A}$. They indicate that, except for the depth range 2550-2700 km at NP, which might be sampled by fewer raypaths due to the geometry of the NP dataset, our models provide a good sampling of the region we explored. In our case, the unknown parameters are V_S (SH-wave) and Q_S in the depth range of 2000–2891 km, and with a vertical interval of 50 km. Finally, to solve Eq. (1), we used the conjugate gradient method, which takes into account the Hessian matrix, theoretical sensitivity, and the gradient direction that the data indicates in first approximation.

2.2. Radial models

Radial models of dlnV_S (with respect to PREM) and Q_S are plotted in Fig. 3. At NP, V_S and Q_S remain slightly lower than PREM throughout the investigated depth-range, with dlnV_S $\sim$ -0.1% and Q_S $\sim$ 300 (compared to $Q_{PREM} = 312$). In this region, the V_S observed by global tomographic maps are close to PREM, either slightly slower (Ritsema et al., 2011), as in our model, or slightly faster (Houser et al., 2008; Moulik and Ekström, 2016). At WP, by contrast, both V_S and Q_S are substantially lower than PREM. In the lowermost 500 km, dlnV_S and Q_S sharply decrease, from -0.6% and 255 at 2500 km, to -2.5% and 215 close to the CMB. These values of dlnV_S are in good agreement with global tomographic maps at these depths (e.g., Houser et al., 2008; Ritsema et al., 2011; Moulik and Ekström, 2016). Coloured areas in Fig. 3 denote uncertainties in dlnV_S and Q_S, which, based on resolution and bootstrap tests (next paragraph), we estimated to be 0.1% and 15, respectively. These uncertainties do not account for errors related to propagation effects, in particular focussing or defocussing. In our case, these biases may however be limited (section 3.4).

To evaluate the vertical resolution of our models, we performed a series of noise-free checkerboard tests (Fig. 4). At each location, these tests consist of four target models (black lines), for which we determined a synthetic dataset using PREM as starting model. We then inverted these datasets for synthetic models at WP (green lines) and NP (red lines) with source–receiver configurations similar to those of the real dataset. The first test model (first row in Fig. 4) is a standard checkerboard test with five layers, in which
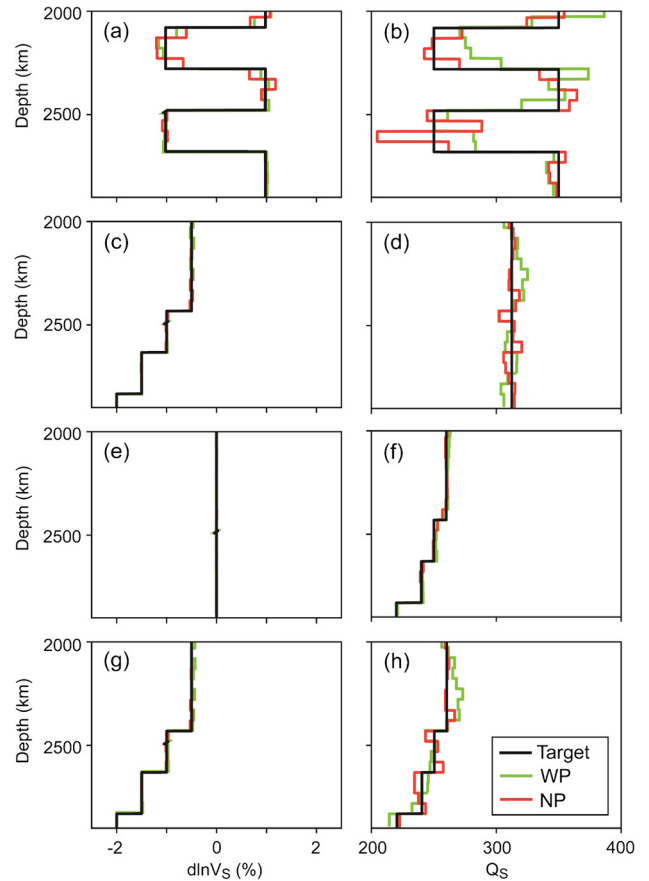

Fig. 4. Checkerboard tests for Western Pacific (WP) and Northern Pacific (NP) models. Black lines show target models, and green and red lines plot output models at WP and NP, respectively. Each row represents one test, with left and right panels showing models of V_S-anomalies (dlnV_S) and Q_S, respectively. The models of dlnV_S are shown in percentage relative to PREM (Dziewonski and Anderson, 1981).

V_S is alternatively faster and slower than PREM by 1%, and Q_S alternatively equal to 350 and 250. Synthetic models suggest that V_S-anomalies are well resolved at depths larger than 2500 km, and are affected by a slight trade-off between dlnV_S and Q_S at shallower depths. Q_S is affected by larger trade-offs throughout the depth range 2000–2850 km, but its radial structure is globally well recovered. The three other target models are more specifically designed to check whether the anomalies we observe are well resolved. They consist of simplified versions of the WP models obtained from real data. In the second and third test models (second and third rows in Fig. 4), we imposed perturbations either in V_S or Q_S, and fixed the other parameter to its PREM value. In the fourth target models (bottom row in Fig. 4), we imposed both V_S and Q_S perturbations. These tests show that the V_S structure is very well resolved throughout the depth range we explored, with deviations in dlnV_S lower than 0.1%. The radial structure of Q_S is affected by moderate trade-offs between depths of 2000 and 2600 km, but is overall well recovered, with maximum deviations around 10 at WP, and even less at NP (Fig. 4). We further conducted bootstrap tests, in which we inverted selected waveforms for a collection of 100 perturbed models. Each perturbed model is calculated with similar conditions as our radial models but uses only 50% of the waveforms of our original datasets, the selected waveforms being randomly chosen. Perturbed models of dlnV_S and Q_S (Supplementary Fig. S3) deviate from the models obtained with full datasets by less than 0.1% and 10, respectively. Overall, resolution and bootstrap tests suggest that our radial models of dlnV_S and Q_S are robust and are only affected by limited uncertainties.

3. Origin of shear-wave speed and attenuation anomalies

The deviations of V_S and Q_S from the PREM values observed at WP and NP may originate from anomalies in temperature and possibly composition. A careful modelling of V_S and Q_S, which we detail in this section, gives access to the temperature anomalies needed to explain these deviations at a given depth. Comparison between the temperature anomalies predicted by $dln V_S$ and Q_S then provides information on the origin of these anomalies (Supplementary Fig. S4). In section 4, we use this procedure to build radial thermo-chemical models at WP and NP.

3.1. Modelling of shear-wave speed anomalies

Shear-wave speed varies with temperature and composition. In the lower mantle, chemical contributions to seismic velocity anomalies may include lateral variations in the global fraction of iron oxide (FeO), in the relative fractions of bridgmanite and ferropericlase, and in the stability field of the post-perovskite (pPv) phase. Recycled oceanic crust (MORB) may reach the deep mantle and add some compositional heterogeneity. It has further been suggested that LLSVPs are layered structures consisting of a deep layer of primordial material overlain by recycled, less dense basaltic material (Ballmer et al., 2016). Here, we assume that the chemical contribution to $dln V_S$ is dominated by variations in the global fraction of FeO, and in the stability field of the pPv phase. LLSVPs may further be enriched in bridgmanite (Trampert et al., 2004; Mosca et al., 2012), and plumes may entrain small fractions of recycled oceanic crust (Tackley, 2012; Li et al., 2014a). These potential sources of heterogeneity would contribute to the observed $dln V_S$, but for simplicity we did not account for them. It should be noted, however, that both an excess of bridgmanite in LLSVPs and the presence of recycled oceanic crust in plumes would slightly increase V_S in these regions (Deschamps et al., 2012), i.e. have the opposite effect of an excess in temperature or iron. Small fractions of recycled MORB may also be incorporated in LLSVPs (Tackley, 2012). However, because shear-wave speed increases with increasing fraction of MORB (Deschamps et al., 2012), LLSVPs are unlikely composed of recycled MORB only, as the shear-wave speed anomalies ($dln V_S$) observed in these structures would imply unrealistic temperature excess, around 1500 K and more.

Assuming that the $dln V_S$ we observe at NP and WP are affected by variations in temperature and in the fractions of FeO, dx_{Fe}, and pPv, dX_{pPv}, the temperature anomalies can be derived from the observed $dln V_S$ and the assumed compositional model (dx_{Fe} and dX_{pPv}) following

$$dT_{V_S} = \frac{(dln V_S - S_{Fe}dx_{Fe} - S_{pPv}dX_{pPv})}{S_T}, \tag{2}$$

with different compositional models leading to different estimates of dT_{V_S}. In Eq. (2), S_T and S_{Fe} are sensitivities of shear-wave speed to temperature and iron, here taken from Deschamps et al. (2012) (Supplementary Fig. S5), while the sensitivity to pPv, S_{pPv}, is based on a recent compilation of mineral physics data (Cobden et al., 2015), and is fixed to $(2.0 \pm 1.0) \times 10^{-2}$ throughout the depth range 2000–2891 km.

A difficulty in solving Eq. (2) is that, because the stability field of pPv depends on both temperature and pressure, the local and reference (horizontally averaged) fractions of pPv, X_{pPv} and $X_{pPv,ref}$, depend on the local and horizontally averaged temperatures, i.e., dX_{pPv} depends on dT_{VS}. We accounted for these dependences by modifying Eq. (2) following (Supplementary Material)

$$dT_{V_S} = \frac{(dln V_S - S_{Fe}dx_{Fe})}{S_T}$$
$$- \frac{S_{pPv}}{2S_T}\left[1 - \tanh\left(\frac{T_{ref} + dT_{VS} - T_{pPv}}{\delta T_{pPv}}\right)\right], \tag{3}$$

where T_{pPv} is the temperature of the transition from bridgmanite to pPv, and δT_{pPv} a typical temperature anomaly modelling the thermal width of the transition and the temperature variation within the volume considered. Here, we fixed δT_{pPv} to 20 K, and based on the compilation of Cobden et al. (2015) we assumed that $T_{pPv} = 3150$ K at $z = 2850$ km. Equation (3) must then be solved for dT_{VS}, which we did using a Newton-Raphson zero search method. The knowledge of dT_{VS} at given location and reference temperature then gives access to the anomaly dX_{pPv} at this location (Supplementary Material).

3.2. Modelling of quality factor anomalies

To estimate temperature anomalies from quality factor Q_S, we followed a classical approach assuming that attenuation is a thermally activated process with a relaxation time modelled with an Arrhenius law (Anderson and Given, 1982). If attenuation is small enough, the quality factor follows a power-law, with exponent α, of the frequency ω and of the relaxation time (Minster and Anderson, 1981). The frequency dependence of seismic attenuation follows an absorption band model (Anderson and Given, 1982), in which attenuation is high only within a frequency band, and sharply decreases outside this absorption band. In addition, within the absorption band attenuation does not substantially vary with frequency. Taking into account the possible effect of grain size (Jackson et al., 2002), the quality factor can be written

$$Q_S = Q_0 d^m \omega^\alpha \exp\left(\alpha\frac{H}{RT}\right), \tag{4}$$

where Q_0 is a constant, d the grain-size, R the ideal gas constant, T the temperature, and $H = E + pV$ the activation enthalpy, with E and V being the activation energy and volume, respectively, and p the pressure. Because activation volume is positive, H increases with depth. The sensitivity to grain-size is controlled by the exponent m, which has been estimated to be $m = 0.24$ for polycrystalline olivine (Jackson et al., 2002). For lower mantle minerals, grain-size sensitivity remains unconstrained. However, since we quantify anomalies in quality factor as $ln(Q_S/Q_{ref})$, where Q_{ref} is a reference quality factor, grain-size effects should not affect our results, provided that it does not vary substantially within the region we explored. Attenuation may depend on the presence of volatiles, most particularly water, but because the amount of volatiles in the deep mantle may be limited (Panero et al., 2015), we did not account for this effect. Based on experimental data (Supplementary Material) and on the modelling of Dannberg et al. (2017), we assumed that lower mantle activation energy and activation volume are in the ranges 280–380 kJ/mol and 1.1×10^{-6}–1.3×10^{-6} m^3/mol, respectively. At lowermost mantle pressure, this leads to activation enthalpy in the range 420–570 kJ/mol. Note that the activation energy of bridgmanite and ferropericlase may differ by a few tens of kJ/mol, with E_{Bm} around 300 kJ/mol, and E_{Fp} around 230 kJ/mol. This may lead to small changes in Q_S with variations in the relative fractions of bridgmanite and ferropericlase, which we did not account for here. An enrichment of LLSVPs in bridgmanite by 10%, as suggested by probabilistic tomography (Trampert et al., 2004), would result in values of H slightly larger than the one we use, reducing the predicted temperature anomalies (see below and Eq. (6)). The

frequency-dependence of attenuation is controlled by the exponent α. A compilation of available body-waves studies indicated that in the Earth's mantle, α should be in the range 0.1–1.0 (Romanowicz and Mitchell, 2015). In the shallow mantle, α was found to be different in the lithosphere, around 0.1, and in the asthenosphere, around 0.3, pointing out that this parameter possibly depends on rheology (Cobden et al., 2018). At lowermost mantle depths, and based on seismic data with seismic-wave periods P in the range 80–3000 s, α was found to be equal to -0.4 for $P \geq 1000$ s, 0.1 for $300 \leq P \leq 800$ s, and around 0.3 for $P \leq 200$ s (Lekić et al., 2009). This frequency dependence is consistent with the absorption band model (Anderson and Given, 1982). In their modelling, Dannberg et al. (2017) used $\alpha = 0.274$, i.e., a value close to that observed by Lekić et al. (2009) for $P \leq 200$ s. Because our models are built for periods in the range 12.5–200 s, and to remain consistent with Dannberg et al. (2017), from which we take values of activation volume, we fixed α to 0.274 in most of our calculations and did additional calculations for $\alpha = 0.2$ and $\alpha = 0.4$ to account for possible uncertainties in α. Assuming that it mainly depends on temperature and that it is not substantially affected by composition, Q_S can be calculated with respect to a reference quality factor Q_{ref} taken at a reference temperature T_{ref} by

$$Q_S(T) = Q_{ref} \exp\left[-\frac{\alpha H}{RT_{ref}} \frac{dT_Q}{(T_{ref} + dT_Q)} \right], \qquad (5)$$

where dT_Q is the temperature anomaly with respect to T_{ref}. Following Eq. (5), and knowing Q_S, this anomaly is given by

$$dT_Q = -\frac{RT_{ref}^2}{\alpha H} \frac{\ln\left(\frac{Q_S}{Q_{ref}}\right)}{[1 + \frac{RT_{ref}}{\alpha H} \ln\left(\frac{Q_S}{Q_{ref}}\right)]}. \qquad (6)$$

Here, we set Q_{ref} to its PREM value, $Q_{PREM} = 312$, and we identify the reference temperature T_{ref} to the mantle geotherm, which is still poorly known. Close to the CMB, a conservative range for T_{ref} is 3000–4000 K (Tackley, 2012). At shallower depths, T_{ref} may be estimated by removing from its CMB value a super-adiabatic temperature jump of 500 K in the lowermost 200 km, modelling the mantle thermal boundary layer, and an adiabatic gradient of 0.3 K/km. A close examination of Eq. (6) shows that dT_Q increases with increasing T_{ref} and decreasing α, but decreases with decreasing H (see also Fig. 5).

3.3. Possible origin of shear-wave speed and quality factor anomalies

A successful description of the mantle thermo-chemical state at a given location requires that for a set of observed $d\ln V_S$ and Q_S, dT_{VS} and dT_Q are equal within their uncertainties. Because activation enthalpy H, reference temperature T_{ref}, and exponent α trade off in the determination of dT_Q, these parameters can always be chosen such that $dT_Q = dT_{VS}$. In practice, however, the range of their possible values is restricted. Even if uncertainties are large, estimates of H and T_{ref} for Earth's mantle are available (section 3.2) and should be satisfied.

At WP and $z = 2850$ km, a purely thermal origin of $d\ln V_S$ leads to dT_{VS} values in the range 800–1040 K (Fig. 5b). Such a high dT_Q requires values of H, T_{ref} or α close to or outside their likely range. For instance, assuming $Q_S = 215$, $T_{ref} = 4000$ K and $\alpha = 0.2$, dT_Q is larger than 800 K only if $H \leq 380$ kJ/mol. For $Q_S = 200$, H rises to 440 kJ/mol, which fits within its possible range for the lower mantle. Accounting for a $dX_{pPv} = -15\%$ depletion of LLSVP in pPv (Supplementary Material), dT_{VS} is in the range 650–980 K, and can be explained by observed attenuation for a narrow range of H, still with $\alpha = 0.2$ and $T_{ref} = 4000$ K. However, because pPv may not be stable in the CMB region for such high values of T_{ref},
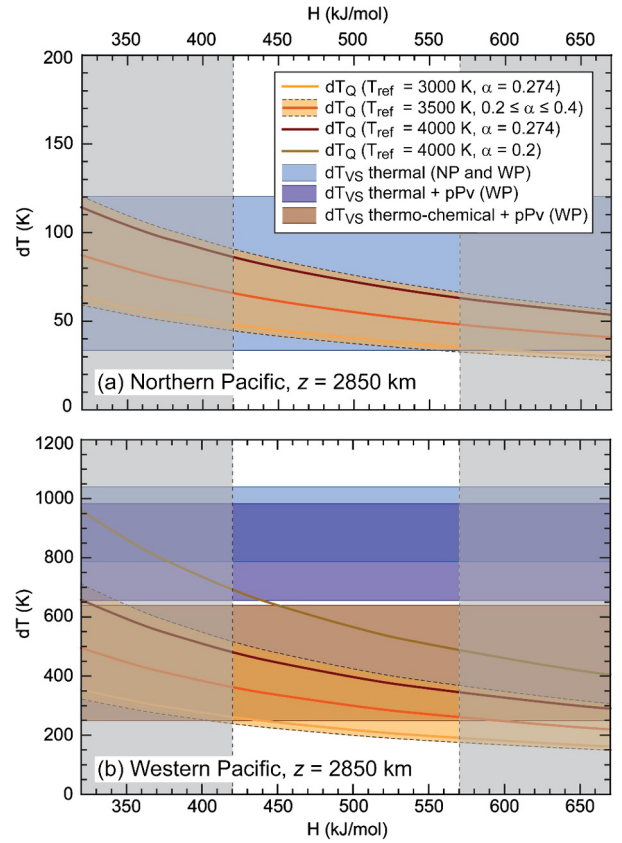

Fig. 5. Temperature anomalies dT_Q (Eq. (6)) inferred from observed shear-wave quality factor (Q_S) at $z = 2850$ km as a function of the activation enthalpy, H, and for several values of the reference temperature T_{ref} and exponent α. Uncertainties in Q_S are not accounted for. Horizontal coloured bands show the temperature anomalies dT_{VS} (Eq. (3)) inferred from observed shear-wave speed anomalies ($d\ln V_S$) at $z = 2850$ km. The width of each band, representing the uncertainty in dT_{VS}, is based on error bars in seismic sensitivities and in observations. (a) Northern Pacific (NP), with $Q_S = 290$ and $d\ln V_S = -0.2\%$. (b) Western Pacific (WP), with $Q_S = 215$ and $d\ln V_S = -2.5\%$. At WP, three *a-priori* thermo-chemical models are considered to estimate dT_{VS}: purely thermal without or with post-perovskite depletion ($dX_{pPv} = -15\%$), and thermo-chemical with post-perovskite depletion ($dX_{pPv} = -15\%$). In this later case, the chemical source has an enrichment in iron with $dx_{Fe} = 3.5\%$. A fourth case (not shown here), with $dx_{Fe} = 3.5\%$ and no variation in post-perovskite, leads to dT_{VS} in the range 400–700 K. The vertical grey shaded bands indicates the range of H that may be excluded (see main text and Supplementary Material).

this case is unlikely. By contrast, assuming that, at WP, the Pacific LLSVP is enriched in iron by $\sim 3.5\%$, as suggested by probabilistic tomography (Trampert et al., 2004; Mosca et al., 2012), and free of pPv, dT_{VS} is between 250 and 640 K and can be explained by a wide range of H, T_{ref} and α. If depletion in pPv is not accounted for (not shown in Fig. 5b) dT_{VS} is larger, in the range 400–700 K, which requires either larger T_{ref}, or smaller values of H and/or α. At NP, the dT_{VS} predicted by a purely thermal $d\ln V_S$ is in the range 35–120 K and can be explained by a wide range of H, T_{ref} and α (Fig. 5a).

A more detailed comparison between dT_{VS} and dT_Q should take into account the variations of post-perovskite anomalies with T_{ref} and the uncertainties in dT_Q due to uncertainties in Q_S. The misfit between dT_{VS} and dT_Q, can then be measured with

$$\chi = \frac{|dT_{VS} - dT_Q|}{(\sigma_{dT,VS} + \sigma_{dT,Q})}, \qquad (7)$$

where $\sigma_{dT,VS}$ and $\sigma_{dT,Q}$ are uncertainties in dT_{VS} and dT_Q. Following this definition, a value of χ larger than 1 indicates that dT_{VS} and dT_Q disagree within their estimated error bars. At NP, temperature anomalies estimated from purely thermal $d\ln V_S$ and
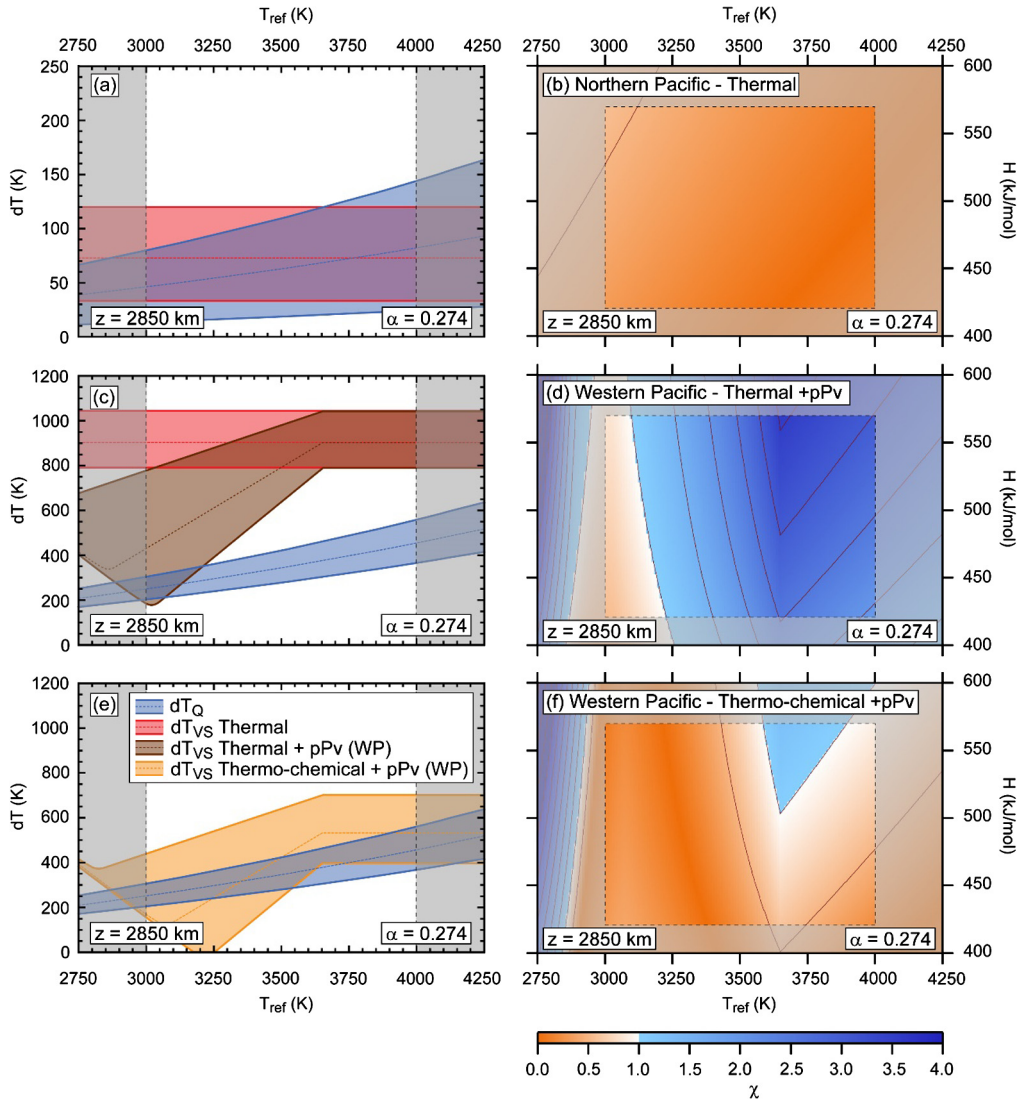
Fig. 6. Left column: temperature anomalies derived from seismic attenuation (dT_Q, Eq. (6)) and shear-wave velocity (dT_{VS}, Eq. (3)) as a function of reference temperature (T_{ref}). For each case, dotted curves and coloured areas represent the average and uncertainties in dT_Q and dT_{VS}. Right column: misfit function between and dT_Q and dT_{VS} (χ, Eq. (7)) as a function of T_{ref} and activation enthalpy (H). Values of χ larger than 1 indicate that dT_Q and dT_{VS} disagree within their error bars. Locations are Northern Pacific (NP, plots a and b), and Western Pacific (plots c to f). At NP, shear-wave velocity anomalies are assumed to have a purely thermal origin. At WP, three possible origin are tested: purely thermal with or without post-perovskite (plots c and d), and thermo-chemical with post-perovskite (plots e and f). All calculations are made at $z = 2850$ km and for a frequency exponent $\alpha = 0.274$ (for other values of α, see Supplementary Figs. S8 and S9). Grey shaded areas indicate the ranges of T_{ref} and H that may be excluded (see main text and Supplementary Material).

from Q_S are consistent for the whole ranges of T_{ref} and H we explored and the values of α we tested (Fig. 6, and Supplementary Figs. S8 and S9). At WP by contrast, dT_{VS} for purely thermal $d\ln V_S$ and dT_Q cannot be reconciled within error bars, except for a very narrow range of T_{ref} at $\alpha = 0.2$ (Fig. S8c). If the presence of pPv is accounted for, the evolution of dT_{VS} with T_{ref} is controlled by changes in dX_{pPv} (Supplementary Material). For $T_{ref} \geq 3650$ K, the entire CMB region is free of pPv, i.e. $dX_{pPv} = 0$ and dT_{VS} is equal to its purely thermal value. At smaller T_{ref}, pPv may be locally stable. The reference fraction of pPv, $X_{pPv,ref}$, increases as T_{ref} decreases, and the depletion in pPv at WP starts increasing. Note that if T_{ref} is small enough (typically in the range 3000–3200 K, depending on the composition at WP), pPv may be stable around WP, in which case dX_{pPv} decreases again. Whenever dX_{pPv} is negative, part of the observed $d\ln V_S$ is explained by this depletion, and the estimated dT_{VS} is reduced compared to its purely thermal value. As a result, for $\alpha = 0.274$, dT_{VS} and dT_Q agree for values of T_{ref} between 2800 and 3200 K, i.e. on the lower end of its pos-

sible values. For $\alpha = 0.2$, this range extends up to T_{ref}=3450 K. Assuming that $d\ln V_S$ at WP are partly due to an excess in iron, here fixed to $dx_{Fe} = 3.5\%$, dT_{VS} and dT_Q now agree for nearly the whole ranges of possible T_{ref} and H at $\alpha = 0.274$ (Figs. 6e and 6f), and for their entire range at $\alpha = 0.2$ (Figs. S8e and S8f). Finally, it is interesting to note that for $\alpha = 0.4$, dT_{VS} and dT_Q are consistent only if WP is enriched in iron and for $T_{ref} \leq 3500$ K (Fig. S9).

Figs. 5 and 6 thus demonstrate that simultaneously explaining shear-wave speed anomalies and attenuation at the western tip of the Pacific LLSVP most likely requires a change in composition that is satisfied by an enrichment in iron by a few percent compared to average mantle. It should further be pointed that our estimates do not account for the presence of small amounts of MORB in LLSVPs or an enrichment of these structures in bridgmanite, and that accounting for these effects would increase the temperature excess compared to our estimates (section 3.1). We now discuss possible bias affecting our radial models and thermo-chemical interpretations.
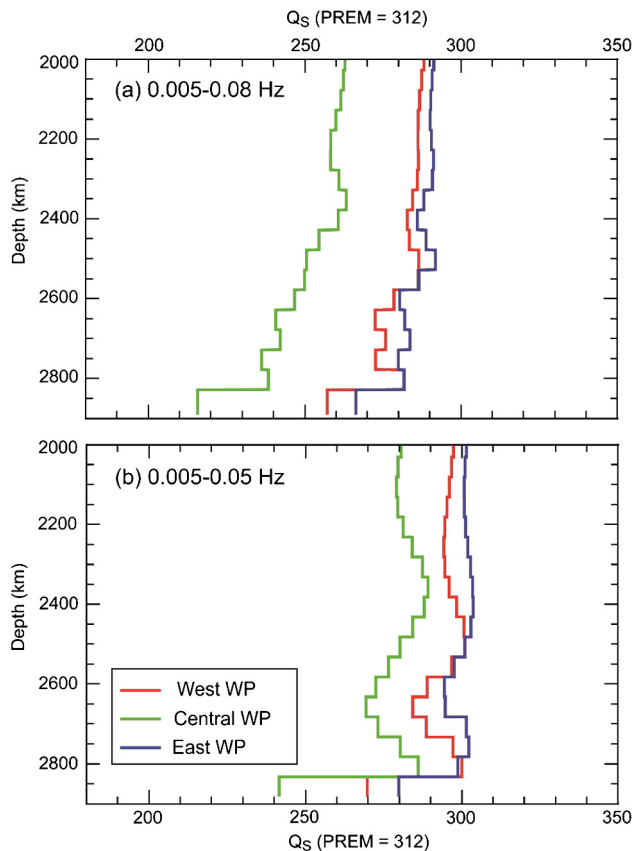
Fig. 7. Models of seismic shear-wave quality factor (Q_S) for the three Western Pacific (WP) sub-regions defined by Konishi et al. (2017), and in two frequency ranges. (a) Frequency range is 0.005–0.08 Hz (12.5–200 s), similar to Konishi et al. (2017). (b) Frequency range is 0.005–0.05 Hz (20–200 s). The WP model used in this study (see Fig. 3) is the central model obtain at 0.005-0.08 Hz (green curve in plot a).

3.4. Focussing effects and seismic anisotropy

A potential bias affecting our quality factor measurements at WP is the focussing or defocussing of seismic rays. Such effects appear in regions where sharp seismic velocity changes are present, and result in underestimating attenuation (measured Q_S is larger than real value) in the case of focussing, or overestimating it (measured Q_S is lower than real value) for defocussing. Focussing may be particularly important for S_{diff} phases travelling through ultra-low velocity zones (ULVZ) (Cottaar and Romanowicz, 2012). It has also been advocated to explain the unusual combination of high Q_S and low V_S observed in the Tonga-Fiji region from ScS_2/ScS measurements (Chaves and Ritsema, 2016). Because our inversion method is based on solving the equation of wave propagation (section 2.1), it implicitly accounts for scattering effects. Intrinsic and scattered contributions to energy loss are thus separated, i.e., our resulting Q_S models, measuring intrinsic attenuation, are not affected by focussing/defocussing effects. This property is supported by the observation that both Q_S and V_S are lower in the central WP region than on its sides (Konishi et al., 2017), i.e., regional trends in V_S and Q_S are similar, while focussing may lead to opposite trend (Chaves and Ritsema, 2016). Preliminary inversion for 3-D structure in this region further indicates that V_S and Q_S variations are well correlated (Konishi et al., 2018). To further investigate the reliability of our Q_S models, and because focussing is expected to decrease with decreasing frequency, we conducted an additional inversion for the three WP sub-regions in the frequency range 0.005–0.05 Hz (period range 20–200 s) (Fig. 7). In this frequency range Q_S is larger than in the range 0.005–0.08 Hz, while one would expect the opposite trend if our models are affected

by focussing. In addition, the regional trends in Q_S are unchanged, i.e., Q_S is lower in the central WP region than on its edges. These results strongly suggest that our Q_S model is not affected by focussing. From Fig. 7, defocussing effects cannot be excluded, but the observation that trends in Q_S are unchanged suggests, again, that they would be limited. Even if substantial defocussing effects are present, the real Q_S would be larger than the value we observe, and the temperature anomaly inferred from it would be even more difficult to reconcile with the temperature anomaly predicted by V_S-anomalies.

Due to similarity in the azimuths of the events-stations paths of our databases, our V_S models may be biased by azimuthal anisotropy, if present in the regions we explored. In the past decades, evidence for seismic anisotropy in the lowermost 200–300 km, potentially related to the arrival and bending of slabs, has accumulated (for a recent review, see Romanowicz and Wenk, 2017). Interestingly, the interiors of LLSVPs appear to be mostly isotropic (Romanowicz and Wenk, 2017). Our WP models may therefore not be affected by anisotropy, leaving unaltered the conclusion that $dlnV_S$ values observed in this region are unlikely purely thermal in origin. We further note that the value of $dlnV_S$ we found at WP fits well within the range of values mapped by global tomography models in this region, which, due to differences in the data and regularization used in each model, vary from −1.5% (Moulik and Ekström, 2016) to −3.1% (French and Romanowicz, 2015), and that it is close to the anomalies observed by Houser et al. (2008) and Ritsema et al. (2011), around −2.3%. By contrast, substantial anisotropy has been reported in the Northern Pacific, potentially altering our NP models. In particular, Wookey et al. (2005) observed ScS splitting equivalent to azimuthal anisotropy with south-eastern direction of fast propagation, i.e. nearly perpendicular to the azimuth of our rays, and amplitude of 0.7–2.3%. If correct, this observation implies that V_S in this region is faster than our estimate, with anomalies (compared to PREM) around 1.0%. Such values can however be reconciled with the small temperature excess predicted by our Q_S models if, as assumed by Wookey et al. (2005), anisotropy in this region is related to slab deflection above the CMB. Because high pressure MORBs are intrinsically slightly faster than pyrolitic material (Deschamps et al., 2012), a 50 K temperature excess would result in a V_S-anomaly around 1.0% or more, depending on the volume fraction of MORB.

4. Radial thermo-chemical structure

We then estimated radial models of temperature anomalies at WP and NP independently from our models of Q_S and $dlnV_S$. Computing dT_Q models requires the definition of a depth-dependent model for T_{ref} and H, while calculating dT_{VS} needs the prescription of a priori radial models of anomalies in iron and post-perovskite (Supplementary Material, Fig. S10). The radial model of H is based, again, on the modelling of Dannberg et al. (2017). The mean model assumes activation energy $E = 286$ kJ/mol and activation volume $V = 1.1 \times 10^{-6}$ m^3/mol, and error bars are obtained by varying these parameters within 280–380 kJ/mol and 1.1×10^{-6}–1.3×10^{-6} m^3/mol, respectively. The model of T_{ref} accounts for the presence of a thermal boundary layer at the bottom of the mantle, and of a regular adiabatic decrease of temperature with altitude of 0.3 K/km. The temperature at CMB is fixed to 3500 K, and because the mantle geotherm is poorly constrained, we imposed error bars of ±500 K at all depths. We further accounted for uncertainties in Q_S and $dlnV_S$ estimated from resolution and bootstrap tests (Fig. 4 and Supplementary Fig. S3), and in seismic sensitivities (Supplementary Fig. S5). The post-perovskite (pPv) model we use is very simple and may slightly affect the dT_{VS} we infer in the depth range 2700–2850 km. This, however, would not alter our main conclusions (Supplementary Material). More impor-
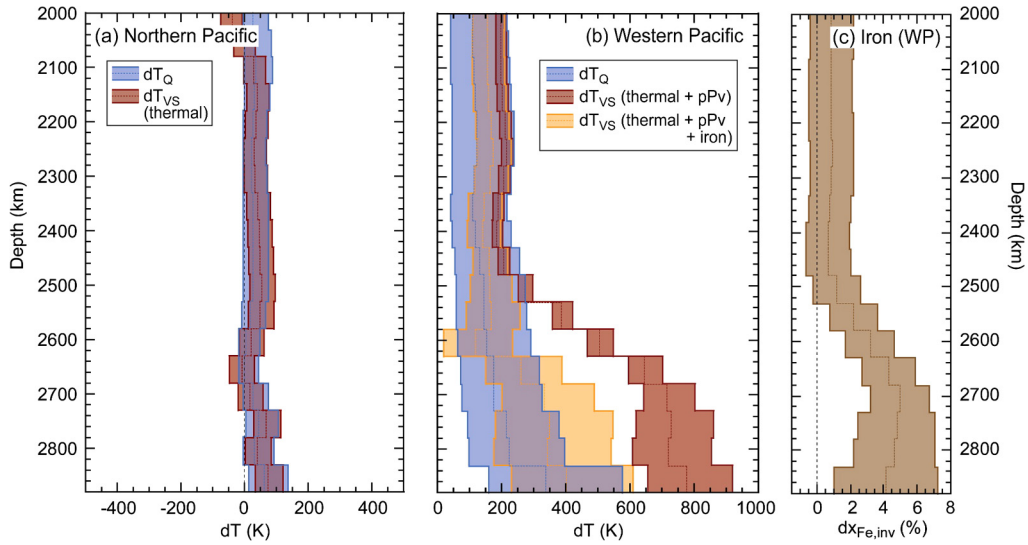
Fig. 8. (a and b) Radial models of temperature anomalies inferred from profiles of shear velocity anomalies ($dln V_S$, red and orange curves and shades) and shear-wave attenuation (Q_S, blue curves and shades) plotted in Fig. 3. (a) Northern Pacific (NP). (b) Western Pacific (WP). For WP, we considered two possible *a-priori* thermo-chemical models as the origin of $dln V_S$: purely thermal with the presence of post-perovskite in the bottom 150 km (dark red curves and shade); and thermo-chemical, with iron enrichment by 3.5% and 0.4% in the bottom (2600–2850 km) and top (2000–2500 km) part, respectively, and with post-perovskite in the bottom 150 km (orange curves and shade). Radial models of iron and post-perovskite anomalies are shown in Supplementary Figs. S10c and S10d. For NP, we assumed that $dln V_S$ is purely thermal in origin, and that the local fraction of post-perovskite is equal to the horizontal average, i.e., $dX_{pPv} = 0$. For models inferred from Q_S, we assumed $\alpha = 0.274$ and we used models of reference temperature, T_{ref}, and activation enthalpy, H, plotted in Supplementary Figs. S10a and S10b, at both WP and NP. B based on resolution and bootstrap tests (Figs. 4 and Supplementary Fig. S3), we imposed uncertainties of ± 0.1% and ± 15 on observed $dln V_S$ and Q_S. (c) Radial model of iron anomalies $dx_{Fe,inv}$ (Eq. (8)) at WP inferred from the temperature anomalies deduced from Q_S (blue profile in plot b), and assuming the radial model of post-perovskite anomalies in Supplementary Fig. S10d.

tantly, this model assumes a reference pPv fraction of 15%, and larger values of $X_{pPv,ref}$ would increase the contribution of pPv anomalies to the observed $dln V_S$, thus reducing dT_{VS}. However, this would also imply smaller T_{ref} leading to smaller dT_Q, such that values of dT_{VS} and dT_Q are still incompatible (Supplementary Material). Low T_{ref} further implies that pPv might be present within LLSVP, thus decreasing dX_{pPv} and its contribution to $dln V_S$. Finally, if enriched in iron, pPv may be stable at shallower depths and larger temperatures (Mao et al., 2006), and may thus exist within LLSVPs, a possibility that we do not consider. If true, the depletion of LLSVPs in pPv would be, again, reduced, and its contribution to $dln V_S$ would be smaller.

At NP (Fig. 8a), models of dT_Q and dT_{VS} obtained for purely thermal $dln V_S$ are in excellent agreement throughout the depth range we explored. Within error bars, temperature is close to T_{ref}, except in the lowermost 150 km layer, where it is larger by about 50 K. At WP (Fig. 8b), dT_Q is around 120–170 K from 2000 down to 2700 km, and increases to 350 ± 200 K at the CMB. In the lowermost mantle ($z \geq 2500$ km), and within error bars, dT_{VS} obtained for $dx_{Fe} = 0$ and dX_{pPv} from Supplementary Fig. S10d reaches 800 ± 200 K and disagrees with dT_Q. At shallower depths, the mean dT_{VS} is larger than the mean dT_Q by about 100 K, but within error bars these two estimates can still be reconciled. By contrast, if accounting for enrichments in iron of 3.5% in the LLSVP and 0.4% in the Caroline plume conduit (Supplementary Fig. S10c), dT_{VS} is fully consistent with dT_Q at all depths.

Assuming that Q_S is a good proxy for temperature and that the compositional signal in $dln V_S$ is dominated by anomalies in the fraction of iron oxide, we then calculated a radial model of iron anomalies at WP from models of observed $dln V_S$ (Fig. 3a), estimated dT_Q (blue curve in Fig. 8b), and *a priori* post-perovskite anomalies (Supplementary Fig. S10d) following

$$dx_{Fe,inv} = \frac{(dln V_S - S_T dT_Q - S_{pPv} dX_{pPv})}{S_{Fe}}, \qquad (8)$$

where S_T, S_{Fe}, and S_{pPv} are, again, sensitivities of V_S to temperature, iron, and post-perovskite (section 3.1), and anomalies in

post-perovskite, dX_{pPv}, are taken from Supplementary Fig. S10d. Throughout a 300 km thick layer above the CMB, explaining $dln V_S$ requires an iron excess (compared to regular pyrolitic mantle) of 3.5–4.5% on average, depending on depth, with uncertainty around 2.0% (Fig. 8c). These values are consistent with estimates from probabilistic tomography (Trampert et al., 2004; Mosca et al., 2012). At shallower depths, iron excess regularly decreases upwards, reaching ∼0.8% at a depth of 2500 km, but error bars do not exclude a regular composition, with iron content similar to that of the surrounding mantle. This slight enrichment persists throughout the depth range 2000–2500 km.

5. Implication for deep mantle structure and dynamics

At the western tip of the Pacific LLSVP, the combination of a 350 K temperature anomaly, as predicted by dT_Q, and a 3.5–4.5% iron excess, required to explain $dln V_S$, provides an estimate of anomalies in density and compressional-wave speed (V_P). Using sensitivities of density to temperature and iron from Deschamps et al. (2012) averaged out in the depth range 2600–2891 km, and assuming that post-perovskite is denser than bridgmanite by 1.5% (Cobden et al., 2015), this region is denser than PREM by $dln\rho = (0.6 \pm 0.4)\%$ on average, in agreement with recent estimates of density excess in LLSVPs from Earth's solid tides (Lau et al., 2017). While this density excess disagrees with the maximum likelihood of LLSVPs density estimated from Stoneley modes (Koelemeijer et al., 2017), it still provides a reasonable fit to these modes, in particular if all structural degrees are included. Similarly, using sensitivities of V_P to temperature and iron from Deschamps et al. (2012) averaged out in the depth range 2600–2891 km, and assuming that post-perovskite leaves V_P unchanged (Cobden et al., 2015), the relative V_P-anomaly, $dln V_P$, is equal to $(-1.2 \pm 0.4)\%$. This value is slightly larger, but comparable to and consistent with anomalies observed by global models of compressional-wave velocity, around −0.5 to −1.0% (Houser et al., 2008; Moulik and Ekström, 2016). If, as suggested by probabilistic tomography (Trampert et al., 2004; Mosca et al., 2012), LLSVPs are further enriched in bridgmanite by ∼10%, and because V_P slightly increases

with increasing fraction of bridgmanite (Deschamps et al., 2012), $dlnV_P$ gets closer to tomographic values, around -0.6%. It should also be kept in mind that due to regularization, global tomography tends to underestimate the amplitude of velocity anomalies.

A 3.5–4.5% iron excess in LLSVPs induces a chemical density contrast between these structures and the surrounding mantle. This, in turn, promotes their long-term stability, as suggested by numerical simulations of thermo-chemical convection (e.g., McNamara and Zhong, 2004; Li et al., 2014b). The density increase may further induce depression of up to 1–2 km in CMB topography (Deschamps et al., 2018), consistent with the long-wavelength topography observed from *P4KP–PcP* differential traveltimes (Tanaka, 2010). There is however no consensus on the CMB topography pattern and amplitude, and more detailed local and global seismic studies are needed to refine available maps of CMB topography. Note, also, that topography may trade off with observed $dlnV_S$ (Supplementary Material). In the frequency range we use, this effect may, however, be limited. Finally, iron excess in the lowermost mantle, combined with higher temperature, may locally decrease thermal conductivity (Hsieh et al., 2017). More specifically, for a 4.0% enrichment in iron and a 350 K temperature excess, conductivity may decrease by $\sim15\%$. Such low conductivity, combined with higher temperature, would in turn substantially decrease the local CMB heat flux, potentially affecting core dynamics and geodynamo (Olson and Christensen, 2002).

The slight enrichment in iron we inferred in the depth range 2000-2500 km, if real, may be related to the entrainment of small amounts of LLSVP material by the Caroline plume. Geodynamical models (Deschamps et al., 2011) have shown that plumes generated at the top of reservoirs of dense material (modelling LLSVPs) entrain small amounts of this dense material. These models further indicate that for density contrasts leading to stable thermochemical piles, the fraction of dense material within the plume is around 10%, a value that further explains mass balance calculations based on the distribution of Helium isotopic ratios in Ocean Island basalts (Allègre and Moreira, 2004). Plumes rising from LLSVPs may thus be slightly enriched in iron, with volume fraction about one order of magnitude smaller than in the LLSVPs. Given error bars, our inferred radial model of iron excess fits this constraint well, with iron fraction around 3.5–4.5% within the Pacific LLSVP, and $(0.8 \pm 1.0)\%$ within the Caroline plume conduit. We further note that in this depth range, the temperature anomaly inferred from Q_S is around 100–200 K, which agrees very well with temperature excesses within plumes estimated from petrological and isotope geochemistry data (Schilling, 1991), heat flow measurements (Sleep, 1990), and numerical modelling of thermo-chemical plumes (Farnetani, 1997).

6. Conclusion

Applied to the deep mantle, the combination of shear-wave speed anomalies and seismic attenuation models supports a thermo-chemical nature for LLSVPs, at least locally. More specifically, our study shows that, compared to the average mantle, the western tip of the Pacific LLSVP may be hotter by ~350 K and enriched in iron oxide by ~3.5–4.5%, in agreement with estimates from normal modes data (Trampert et al., 2004; Mosca et al., 2012). Independent constraints (normal mode data on one side, and the combination of attenuation and shear-wave velocity anomalies on the other side) thus lead to similar conclusions on the deep mantle thermo-chemical structure. In addition, plumes rising from this region may be enriched in iron by $\sim0.8\%$, possibly because they entrain small amounts of the Pacific LLSVP material upwards. Our method can easily be extended to other regions and to the 3-D mapping of shear-wave speed and seismic attenuation, provided that data are available. Additional studies

addressing different LLSVPs areas should be conducted to check whether our conclusions apply to entire LLSVPs or are limited to part of them, e.g., the base of fat plumes observed by French and Romanowicz (2015). Seismic waveform inversion for shear-wave speed and seismic attenuation thus potentially provides a powerful tool to recover the thermo-chemical structure of the deep Earth's mantle, a conclusion that may further apply to the upper mantle (Cobden et al., 2018).

Appendix A. Supplementary material

Supplementary material related to this article can be found online at https://doi.org/10.1016/j.epsl.2019.05.040.

References

Allègre, C.J., Moreira, M., 2004. Rare gas systematic and the origin of oceanic islands: the key role of entrainment at the 670 km boundary layer. Earth Planet. Sci. Lett. 228, 85–92.

Anderson, D.L., Given, D.W., 1982. Absorption band Q model for the Earth. J. Geophys. Res. 87, 3896–3904.

Ballmer, M.D., Schumacher, L., Lekić, V., Thomas, C., Ito, G., 2016. Compositional layering within the large low shear-wave velocity provinces in the lower mantle. Geochem. Geophys. Geosyst. 17, 5056–5077. https://doi.org/10.1002/2016GC006605.

Bozdağ, E., Peter, D., Lefebvre, M., Komatitsch, D., Tromp, J., Hill, J., Podhorszki, N., Pugmire, D., 2016. Global adjoint-tomography: first generation model. Geophys. J. Int. 207, 1739–1766.

Bull, A.L., McNamara, A.K., Ritsema, J., 2009. Synthetic tomography of plume clusters and thermochemical piles. Earth Planet. Sci. Lett. 278, 152–162.

Chaves, C.A.M., Ritsema, J., 2016. The influence of shear-velocity heterogeneity on ScS_2/ScS amplitude ratios and estimates of Q in the mantle. Geophys. Res. Lett. 43, 7997–8005.

Cobden, L.J., Thomas, C., Trampert, J., 2015. Seismic detection of post-perovskite inside the Earth. In: Khan, A., Deschamps, F. (Eds.), The Earth's Heterogeneous Mantle. Springer, pp. 391–440.

Cobden, L., Trampert, J., Fichtner, A., 2018. Insights on upper mantle melting, rheology and anelastic behaviour from seismic shear-wave tomography. Geochem. Geophys. Geosyst. 19, 3892–3916. https://doi.org/10.1029/2017GC007370.

Cottaar, S., Romanowicz, B., 2012. An unusually large ULVZ at the base of the mantle near Hawaii. Earth Planet. Sci. Lett. 355–356, 213–222.

Dannberg, J., Eilon, Z., Faul, U., Gassmöller, R., Moulik, P., Myhill, R., 2017. The importance of grain size to mantle dynamics and seismological observations. Geochem. Geophys. Geosyst. 18, 3034–3061. https://doi.org/10.1002/2017GC006944.

Davies, D.R., Goes, S., Davies, J.H., Schuberth, B.S.A., Bunge, H.-P., Ritsema, J., 2012. Reconciling dynamic and seismic models of Earth's lower mantle: the dominant role of thermal heterogeneity. Earth Planet. Sci. Lett. 353–354, 253–269.

Deschamps, F., Kaminski, E., Tackley, P.J., 2011. A deep mantle origin for the primitive signature of ocean island basalt. Nat. Geosci. 4, 879–882.

Deschamps, F., Cobden, L., Tackley, P.J., 2012. The primitive nature of large low shear-wave velocity provinces. Earth Planet. Sci. Lett. 349–350, 198–208.

Deschamps, F., Rogister, Y., Tackley, P.J., 2018. Constraints on core-mantle boundary topography from models of thermal and thermo-chemical convection. Geophys. J. Int. 212, 164–188.

Ding, H., Chao, B.F., 2018. A 6-year westward rotary motion in the Earth: detection and possible MICG coupling mechanism. Earth Planet. Sci. Lett. 495, 50–55.

Dziewonski, A.M., Anderson, D.L., 1981. Preliminary reference Earth model. Phys. Earth Planet. Inter. 25, 297–356.

Farnetani, C.G., 1997. Excess temperature of mantle plumes: the role of the chemical stratification across D". Geophys. Res. Lett. 24, 1583–1586.

French, S.W., Romanowicz, B., 2015. Broad plumes rooted at the base of the Earth's mantle beneath major hotspots. Nature 525, 95–99.

Fuji, N., Kawai, K., Geller, R.J., 2010. A methodology for inversion of broadband seismic waveforms for elastic and anelastic structure and its application to the mantle transition zone beneath the northwestern pacific. Phys. Earth Planet. Inter. 180, 118–137.

Garnero, E.J., McNamara, A., Shim, S.-H., 2016. Continent-sized anomalous zones with low seismic velocity at the base of Earth's mantle. Nat. Geosci. 9, 481–489.

Geller, R.J., Ohminato, N., 1994. Computation of synthetic seismograms and their partial derivatives for heterogeneous media with arbitrary natural boundary conditions using the direct solution method. Geophys. J. Int. 116, 421–446.

Houser, C., Masters, G., Shearer, P., Laske, G., 2008. Shear and compressional velocity models of the mantle from cluster analysis of long-period waveforms. Geophys. J. Int. 174, 195–212.

Hsieh, W.-P., Deschamps, F., Okuchi, T., Lin, J.F., 2017. Reduced lattice thermal conductivity of Fe-bearing bridgmanite in Earth's deep mantle. J. Geophys. Res., Solid Earth 122, 4900–4917.

Hutko, A.R., Lay, T., Revenaugh, J., Garnero, E.J., 2008. Anticorrelated seismic velocity anomalies from post-perovskite in the lowermost mantle. Science 320, 1070–1074.

Jackson, I., Fitz Gerald, J.D., Faul, U.H., Tan, B.H., 2002. Grain-size-sensitive seismic wave attenuation in polycrystalline olivine. J. Geophys. Res. 107. https://doi.org/10.1029/2001JB001225.

Koelemeijer, P., Deuss, A., Ritsema, J., 2017. Density structure of Earth's lowermost mantle from Stoneley mode splitting observations. Nat. Commun. 8. https://doi.org/10.1038/ncomms15241.

Konishi, K., Kawai, K., Geller, R.J., Fuji, N., 2009. MORB in the lowermost mantle beneath the western pacific: evidence from waveform inversion. Earth Planet. Sci. Lett. 278, 219–225.

Konishi, K., Fuji, N., Deschamps, F., 2017. Elastic and anelastic structure of the lowermost mantle beneath the Western Pacific from waveform inversion. Geophys. J. Int. 208, 1290–1304.

Konishi, K., Deschamps, F., Fuji, N., 2018. Waveform inversion for the 3-D elastic and anelastic structure of the lowermost mantle beneath the western Pacific. Geophys. Res. Abstr. 20, EGU2018–7336.

Lau, H.C.P., Mitrovica, J.X., Davis, J.L., Tromp, J., Yang, H.-Y., Al-Attar, D., 2017. Tidal tomography constraints Earth's deep mantle buoyancy. Nature 551, 321–326.

Lekić, V., Matas, J., Panning, M., Romanowicz, B., 2009. Measurement and implications of frequency dependence of attenuation. Earth Planet. Sci. Lett. 282, 285–293.

Li, M., McNamara, A.K., Garnero, E.J., 2014a. Chemical complexity of hotspots caused by cycling oceanic crust through mantle reservoirs. Nat. Geosci. 7, 366–370.

Li, Y., Deschamps, F., Tackley, P.J., 2014b. The stability and structure of primordial reservoirs in the lower mantle: insights from models of thermo-chemical convection in 3-D spherical geometry. Geophys. J. Int. 199, 914–930.

Mao, W.L., Mao, H.-K., Sturhahn, W., Zhao, J., Prakapenka, V.B., Meng, Y., Shu, J., Fei, Y., Hemley, R.J., 2006. Iron-rich post-perovskite and the origin of ultralow-velocity zones. Science 312, 564–565.

Masters, G., Laske, G., Bolton, H., Dziewonski, A.M., 2000. The relative behavior of shear velocity, bulk sound speed, and compressional velocity in the mantle: implication for thermal and chemical structure. In: Karato, S.-I., et al. (Eds.), Earth's Deep Interior: Mineral Physics and Tomography from the Atomic to the Global Scale. In: Geophysical Monograph Ser., vol. 117. American Geophysical Union, Washington, DC, pp. 63–87.

McNamara, A.K., Zhong, S., 2004. Thermochemical structures within a spherical mantle. J. Geophys. Res. 109. https://doi.org/10.1029/2003JB002847.

Minster, B., Anderson, D.L., 1981. A model of dislocation-controlled rheology for the mantle. Philos. Trans. R. Soc. A 299, 319–356.

Mosca, I., Cobden, L., Deuss, A., Ritsema, J., Trampert, J., 2012. Seismic and mineralogical structures of the lower mantle from probabilistic tomography. J. Geophys. Res. 117. https://doi.org/10.1029/2011JB008851.

Moulik, P., Ekström, G., 2016. The relationships between large-scale variations in shear velocity, density, and compressional velocity in the Earth's mantle. J. Geophys. Res. 121, 2737–2771.

Olson, P., Christensen, U.R., 2002. The time-averaged magnetic field in numerical dynamos with non-uniform boundary heat flow. Geophys. J. Int. 151, 809–823.

Panero, W.R., Pigott, J.S., Reaman, D.M., Kabbes, J.E., Liu, Z., 2015. Dry (Mg,Fe)SiO$_3$ perovskite in the Earth's lower mantle. J. Geophys. Res., Solid Earth 120, 894–908.

Ritsema, J., Deuss, A., van Heijst, H.-J., Woodhouse, J.H., 2011. S40RTS: a degree-40 shear-velocity model for the mantle from new Rayleigh wave dispersion, teleseismic traveltime and normal-mode splitting function measurements. Geophys. J. Int. 184, 1223–1236.

Romanowicz, B., Mitchell, B.J., 2015. Deep Earth structure: Q of the Earth from core to crust. In: Treatise on Geophysics, vol. 1, 2nd edition, pp. 789–827.

Romanowicz, B., Wenk, H.-R., 2017. Anisotropy in the deep Earth. Phys. Earth Planet. Inter. 269, 58–90.

Schilling, J.-G., 1991. Flux and excess temperatures of mantle plumes inferred from their interaction with migrating mid-ocean ridges. Nature 352, 397–403.

Schuberth, B.S.A., Zaroli, C., Nolet, G., 2012. Synthetic seismograms for a synthetic Earth: long-period P- and S-wave traveltime variations can be explained by temperature alone. Geophys. J. Int. 188, 1393–1412.

Sleep, N.H., 1990. Hotspots and mantle plumes: some phenomenology. J. Geophys. Res. 95, 6715–6736.

Tackley, P.J., 2012. Dynamics and evolution of the deep mantle resulting from thermal, chemical, phase and melting effects. Earth-Sci. Rev. 110, 1–25.

Tanaka, S., 2010. Constraints on the core-mantle boundary topography from P4KP-PcP differential travel times. J. Geophys. Res. 115, B04310. https://doi.org/10.1029/2009JB006563.

Trampert, J., Deschamps, F., Resovsky, J.S., Yuen, D.A., 2004. Probabilistic tomography maps significant chemical heterogeneities in the lower mantle. Science 306, 853–856.

Wookey, J., Kendall, J.-M., Rümpker, G., 2005. Lowermost mantle anisotropy beneath the north Pacific from differential S–ScS splitting. Geophys. J. Int. 161, 829–838.